Neuron, Vol. 34, 685–700, May 30, 2002, Copyright ©2002 by Cell Press

Magnetic Resonance Imaging of Neuronal Connections in the Macaque Monkey

Neurotechnique

Kadharbatcha S. Saleem,[1,3,4] Jon M. Pauls,[2] Mark Augath,[2] Torsten Trinath,[2] Burkhard A. Prause,[2] Tsutomu Hashikawa,[1] and Nikos K. Logothetis[2,3]
[1] Riken Brain Science Institute
2-1 Hirosawa, Wakoshi
Saitama 351-0198
Japan
[2] Max-Planck Institute for Biological Cybernetics
Spemannstrasse 38
72076 Tübingen
Germany

Summary

Recently, an MRI-detectable, neuronal tract-tracing method in living animals was introduced that exploits the anterograde transport of manganese (Mn^{2+}). We present the results of experiments simultaneously tracing manganese chloride and wheat germ agglutinin conjugated to horseradish peroxidase (WGA-HRP) to evaluate the specificity of the former by tracing the neuronal connections of the basal ganglia of the monkey. Mn^{2+} and WGA-HRP yielded remarkably similar and highly specific projection patterns. By showing the sequential transport of Mn^{2+} from striatum to pallidum-substantia nigra and then to thalamus, we demonstrated MRI visualization of transport across at least one synapse in the CNS of the primate. Transsynaptic tract tracing in living primates will allow chronic studies of development and plasticity and provide valuable anatomical information for fMRI and electrophysiological experiments in primates.

Introduction

Until now, neuroanatomical cortico-cortical and cortico-subcortical connections have been examined mainly by means of degeneration methods (Jones and Powell, 1970; Seltzer and Pandya, 1978) and anterograde and retrograde tracing techniques (Saint-Cyr et al., 1990; Baizer et al., 1991; Felleman and Van Essen, 1991; Cheng et al., 1997; Saleem et al., 2000). Neuronal connections have also been investigated to a lesser extent with physiological methods, particularly by means of crosscorrelation analysis of functionally interconnected neurons (Toyama et al., 1981; Aertsen and Gerstein, 1985; Schwarz and Bolz, 1991). Although anatomical tracing studies have demonstrated the value of the information gained from the investigation of the topographic connections between different brain areas, such studies require fixed, processed tissue for data analysis and, therefore, cannot be applied to an animal participating in longitudinal studies where consecutive studies examining an entire circuit could be carried out in the same subjects. In the present work, we examined neuronal connections using an MRI-visible contrast agent that is transported anterogradely through the axon (Sloot and Gramsbergen, 1994) and possibly transported transsynaptically as well (Pautler et al., 1998; Takeda et al., 1998; Henriksson et al., 1999).

The transport and distribution of MRI-visible contrast agents such as manganese (Mn^{2+}) (London et al., 1989; Pautler et al., 1998; Lin et al., 2001; Watanabe et al., 2001; Ryu et al., 2002) and MION (monocrystalline iron oxide nanocompound)-based compounds (Enochs et al., 1993; Van Everdingen et al., 1994) have been studied in rats and mice. With T1-weighted MRI, Pautler et al. (1998) were the first investigators to find a clear signal enhancement in the olfactory and visual pathways of mice after the application of manganese chloride ($MnCl_2$) solution to the naris or its injection into the eye. To study the visual pathway in particular, they used a 0.8 mmol/ml $MnCl_2$ solution for injections into the vitreal chamber of the eye. After 24 hr, they found signal enhancement in the optic tract, as well as in the contralateral superior colliculus. The time course of the enhanced MRI contrast indicated that Mn^{2+} was being transported at approximately 2 mm/hr, consistent with fast axonal transport. Intraocular injection of $MnCl_2$ has also been applied in the rat where labeling was detected in the retina, optic nerve, chiasm, and contralateral optic tract, as well as in a number of central structures including the dorsal and ventral lateral geniculate nucleus and the superior colliculus (Watanabe et al., 2001).

Axonal transport of radioactive manganese ($^{54}Mn^{2+}$) has also been studied using histological methods (Sloot and Gramsbergen, 1994; Tjalve et al., 1995, 1996; Takeda et al., 1998). Sloot and Gramsbergen (1994) showed anterograde transport of radioactive Mn^{2+} after injection into the rat substantia nigra or striatum. They found a region-specific accumulation and retention of the isotope in the globus pallidus, striatum, thalamus, and substantia nigra for up to at least 48 or 72 hr, respectively, suggesting anterograde transport of Mn^{2+}. Although these studies were carried out with the goal of understanding the regional specificity of Mn^{2+} distribution, they clearly indicate the usefulness of Mn^{2+} as an anterograde neuronal tract tracer.

The aim of the research presented here was to study the potential of MRI-detected manganese (Mn^{2+}) transport for the in vivo tracing of the topology of small multisynaptic neural networks in the macaque monkey. We focused particularly—but not exclusively—on the output connections of the striatum in the macaque monkey because these connections, along with other input and output connections of the basal ganglia, have been studied extensively using standard anatomical tracing methods and are firmly established (Ragsdale and Graybiel, 1981; Saint-Cyr et al., 1990; Hedreen and DeLong, 1991; Flaherty and Graybiel, 1993; Parent and Hazrati, 1995a; Cheng et al., 1997). We specifically set out to test the

[3] Correspondence: saleemk@pcg.wustl.edu (K.S.S.), nikos.logothetis@tuebingen.mpg.de (N.K.L.)
[4] Present address: Department of Anatomy and Neurobiology, Washington University School of Medicine, 660 S. Euclid Ave., St. Louis, Missouri 63110.

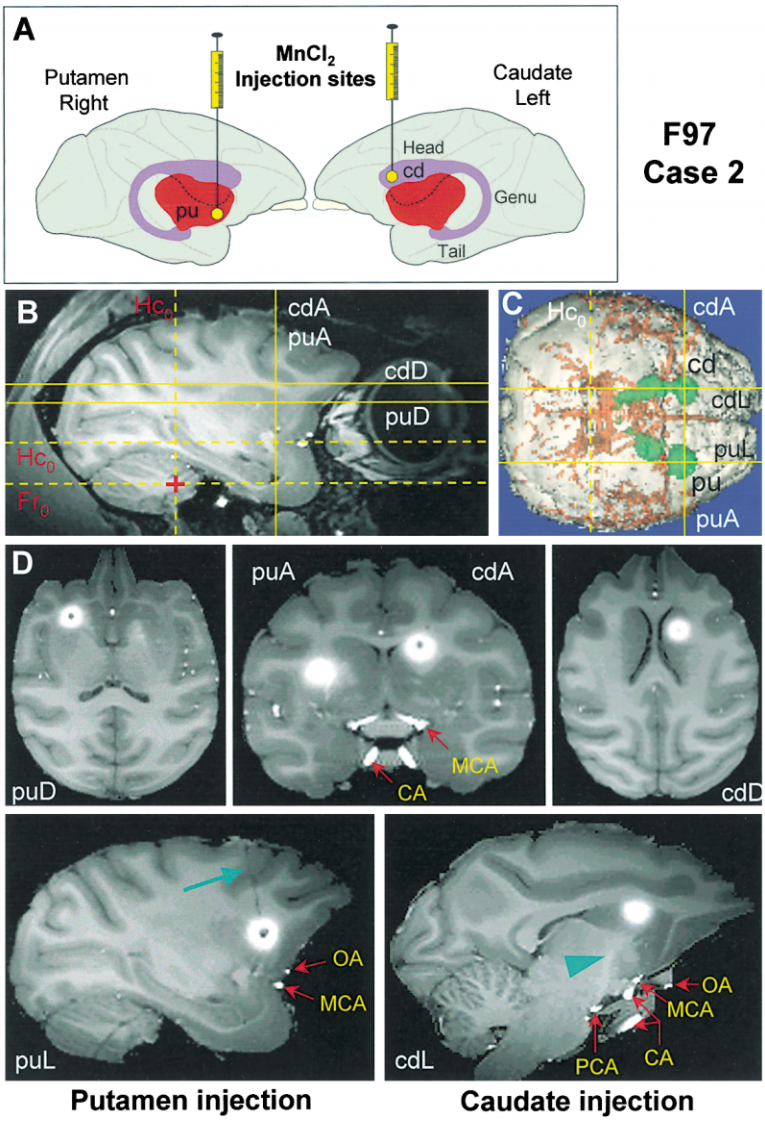

Figure 1. Schematic of Manganese Chloride ($MnCl_2$) Injection Sites and the Actual Injection Sites in the Striatum of Case 2 (F97).

(A) Schematic lateral views of the monkey brain show the injection sites in the rostral part of the right putamen (pu) and the head of the left caudate nucleus (cd).

(B–D) Stereotaxic coordinates for the caudate and putamen injections with respect to the Horsley-Clark (Hc) stereotaxic coordinate system in a sagittal MR image (B) and dorsal view of the rendered brain ([C], 45 hr postinjection) are shown. The horizontal and vertical dashed lines labeled Hc_0 show the horizontal and frontal zero planes, respectively, in the Horsley-Clark system. The solid yellow lines indicate the coordinates of the centers of the caudate and putamen injection sites shown in (D). The red structures in (C) show the brain vasculature as determined by angiography. Blood vessels appear bright white (high signal) in the anatomical scans, as does the manganese (Mn^{2+}) signal (see D). To minimize the error in identifying tracer-containing regions, the signal originating from the vasculature was removed from the anatomical scans by subtracting the corresponding angiography scans. The green structures represent the extents of the Mn^{2+} signal at the sites of the left caudate (cd) and right putamen (pu) injections (spherical regions) and the subsequent path of the tracer in the basal ganglia. The injection coordinates for the caudate were anterior (cdA) 22.0 mm, lateral (cdL) 5 mm, and dorsal (cdD) 13.5 mm. The injection coordinates for the putamen were anterior (puA) 22.0 mm, lateral (puL) 12.5 mm, and dorsal (puD) 9 mm. In (D), the bright regions indicate the spatial extents of the Mn^{2+} signal at the caudate and putamen injection sites in coronal, horizontal, and sagittal MR images at 45 hr postinjection. Both injections were well localized within the corresponding structures. The green arrow (sagittal image, bottom left) indicates the needle penetration tract for the putamen injection. The green arrowhead (sagittal image, bottom right) indicates axonal transport of Mn^{2+} from the caudate injection site. Major blood vessels are labeled with red arrows in the coronal and sagittal images.

Abbreviations: Fr_0, Frankfurt zero plane; CA, carotid artery; MCA, middle cerebral artery; OA, ophthalmic artery; and PCA, posterior cerebral artery.

reliability of manganese-enhanced MRI for tracing neural pathways and the extent to which this tracer is subject to transsynaptic transport. In fact, combined injections of $MnCl_2$ with WGA-HRP yielded remarkably similar projection patterns, suggesting a highly specific transport of the paramagnetic tracer. Most importantly, the spatio-temporal evolution of tracer transport from the striatum to the pallidum-substantia nigra and then to thalamus showed that manganese can indeed cross synapses in the central nervous system and, therefore, be used to delineate multisynaptic networks in the living animal. Preliminary results from this work have been presented elsewhere (K.S. Saleem et al., 2001, Soc. Neurosci., Abstr.).

Results

The $MnCl_2$ injection sites (Figures 1A–1D) were located in the rostral part of the putamen and the head of the caudate nucleus in all three striatum injection cases (cases 1–3; Table 1). The Mn^{2+} ions diffused away from the point of injection, yielding a strong signal in 697 to 2145 voxels (87–268 μl; for comparison, one voxel is equal to 0.125 μl) surrounding the injection site in the first scan, typically 3–6 hr postinjection. In cases 2 and 3, the extent of the injection were confined to the caudate and putamen and did not spread to adjacent areas. In case 1, some Mn^{2+} signal was visible in the adjacent white matter directly surrounding the caudate and putamen, depending on the amount of tracer injected (Table 1). In case 4, the $MnCl_2$ injection site was mostly confined to area 13 of the right orbitofrontal cortex, except for minor diffusion of the tracer into the dorsolateral prefrontal cortex, where the injection needle was inserted to reach the orbitofrontal cortex.

In order to verify the specificity of Mn^{2+} as a neuronal tracer, WGA-HRP was injected at the same stereotaxic locations as the $MnCl_2$ after the completion of either

Table 1. Manganese Chloride ($MnCl_2$) and WGA-HRP Injections in Different Cases

		Striatum				
		Caudate		Putamen		Cortex
Cases	Tracers	L	R	L	R	area 13
1 (F00)	$MnCl_2$	–	0.5 μl	1.0 μl	–	–
	WGA-HRP	–	0.25 μl	0.25 μl	–	–
2 (F97)	$MnCl_2$	0.1 μl	–	–	0.15 μl	–
	WGA-HRP	0.1 μl	–	–	0.15 μl	–
3 (J00)	$MnCl_2$	–	0.1 μl	0.15 μl	–	–
4 (H00)	$MnCl_2$	–	–	–	–	0.1 μl

The concentration of the $MnCl_2$ solution was 0.8 M and the WGA-HRP solution was 5%. The volume of the tracers injected into the caudate and putamen (cases 1–3) and the orbitofrontal cortex (case 4).
L, left hemisphere; R, right hemisphere.

24.5 (case 1) or 45 (case 2) hr of MRI scanning. The WGA-HRP injection sites were also well localized within the same regions of the caudate and putamen as the $MnCl_2$ injections. There was some diffusion of tracer along the needle penetration tracts in the white matter or in the overlying cortical areas in both cases. The distribution of labeling in the striatal targets (globus pallidus and substantia nigra) was nonetheless very similar for both the $MnCl_2$ and the WGA-HRP injections.

The transport of the tracer was followed for periods ranging from 24.5 hr to 18 days. In the two short-term experiments (up to 45 hr; cases 1 and 2), the time course of Mn^{2+} transport was followed at intervals of a few hours. For case 1, both an anatomical and angiography scan were obtained every 2 hr between 3 and 24.5 hr postinjection, for a total of 11 postinjection scans. For case 2, 14 paired anatomy/angiography scans were obtained at 3 hr intervals between 6 and 45 hr after tracer injection. The extent of the Mn^{2+} signal around the injection sites generally increased over the first 45 hr, ultimately reaching 1437 to 4849 voxels (180–606 μl), depending on the amount injected (see Figure 1D, case 2 at 45 hr: caudate, ~1437 voxels; putamen, 1767 voxels).

In two long-term experiments (up to 18 days; cases

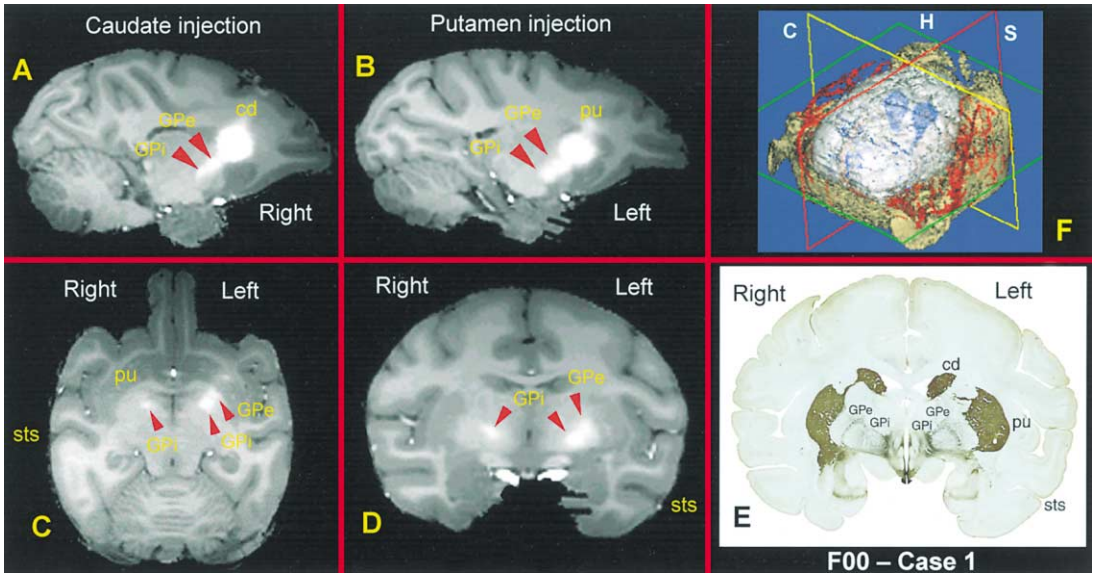

Figure 2. Manganese Transfer to the Globus Pallidus 24.5 hr after Injection into the Caudate and Putamen in Case 1 (F00)

(A and B) Sagittal MR images from right and left hemispheres show the transfer of Mn^{2+} from the sites of injection to the external and internal segments (GPe and GPi, respectively; arrowheads) of the globus pallidus.

(C and D) Horizontal and coronal MR images illustrate the specificity of distribution of Mn^{2+} signal in GPe and GPi (arrowheads). Note the different spatial distributions of the MR-detectable tracer in the globus pallidus (D), precisely as expected, given the known connectivity of striato-pallidal system: the tracer is found in the dorsomedial portion of the GPe and GPi after caudate injection (right hemisphere) and in the ventrolateral or midportion of the GPe and GPi after putamen injection (left hemisphere). Note that at this rostrocaudal level of the globus pallidus, a strong signal was observed only in the GPi on the caudate injection side.

(E) The histological section stained for tyrosine hydroxylase (TH) showing the anatomical borders of the globus pallidus (GPe and GPi) and striatum (cd and pu) is shown. The MR image shown in (D) was matched to the histological section in (E) by rotating and reslicing the volume at the appropriate AP extent using MEDx.

(F) The dorsolateral view of the rendered brain image shows the anatomical locations of the MRI slices in (A), (C), and (D) (red, right sagittal; green, horizontal; and yellow, coronal), the angiography (red structures), and the caudate and putamen injection sites (shown by the blue spheres in the computer-rendered brain).

Abbreviations: cd, caudate nucleus; GPe, globus pallidus external segment; GPi, globus pallidus internal segment; pu, putamen; sts, superior temporal sulcus; S, H, and C: Sagittal, horizontal, and coronal, respectively.

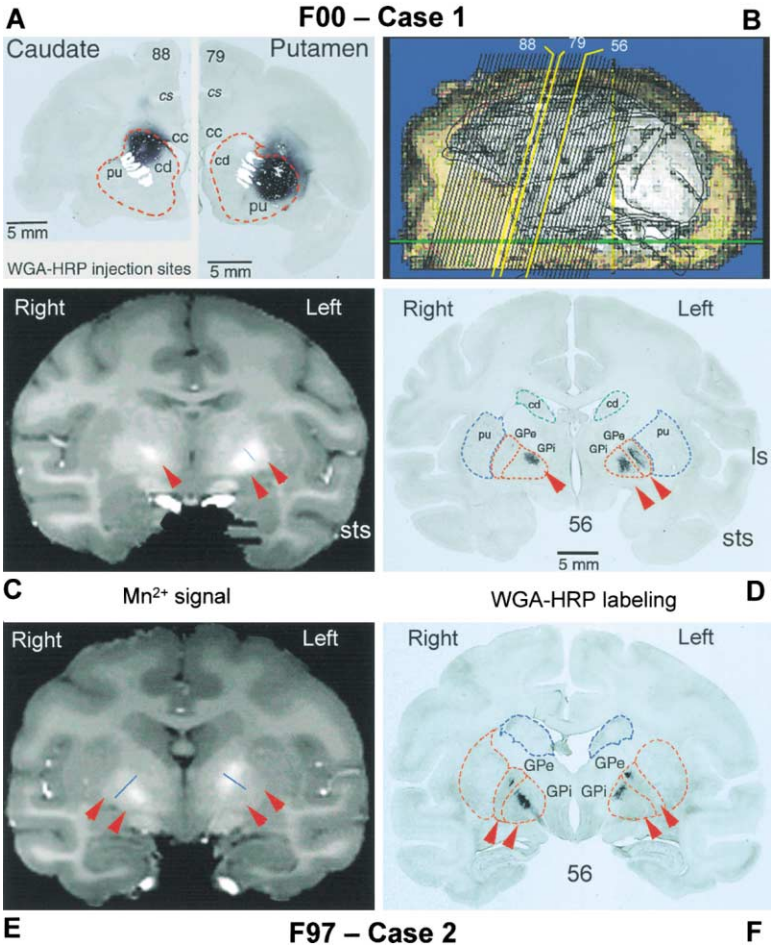

Figure 3. MRI and Histological Visualization of Connections in the Globus Pallidus in Case 1 (F00) and Case 2 (F97)

(A) Coronal histology sections (#79 and #88) illustrate the WGA-HRP injection sites in the left putamen and right caudate nucleus, respectively. WGA-HRP injections were made at the same stereotaxic coordinates as the $MnCl_2$ injections.

(B) The lateral view of the rendered brain shows the rostrocaudal locations of the histology sections shown in (A) and (D) (#79 and #88, #56).

(C and D) Coronal MR image (left) and the coronal histology section (#56, right), respectively, showing the Mn^{2+} signal and WGA-HRP labeling in the GPe and GPi (arrow heads) 24.5 hr after right caudate and left putamen injections. This coronal MR image is the same one shown in Figure 2D. The sulci and other anatomical landmarks are matched in both the MR image and the histology section (#56) to facilitate comparison. Note the similar distribution of Mn^{2+} signal and WGA-HRP labeling in the MR image and the histological section, respectively (arrowheads in GPe and GPi).

(E and F) Coronal MR image and coronal histology section from case 2, respectively, showing the Mn^{2+} signal and WGA-HRP labeling in the GPe and GPi (arrowheads) 45 hr after the injections. In contrast to case 1, the $MnCl_2$/WGA-HRP injections were reversed in this case (right putamen and left caudate injections) (Figure 1; Table 1). All other conventions are as in case 1 (see [C] and [D]).

(A)–(D) refers to case 1, and (E) and (F) refers to case 2.

Abbreviations: CC, corpus callosum; cd, caudate nucleus; cs, cingulate sulcus; GPe, globus pallidus external segment; GPi, globus pallidus internal segment; ls, lateral sulcus; pu, putamen; and sts, superior temporal sulcus.

3 and 4), the progress of the Mn^{2+} signal was followed across at least one synapse after injection in the caudate and opposite putamen (case 3) or orbitofrontal cortex (case 4). Cases 3 and 4 were scanned once before (baseline) and again immediately following their injections. Thereafter, the monkeys were scanned once every 2 days for 8 days (case 4, six scans total), or once every 2 days for 18 days with 3-day intervals between the last three scans (case 3, ten scans total). In case 3, the Mn^{2+} signal intensity around the injection sites first began to decrease after 48 hr postinjection, reaching half-maximum intensity by ~130 and ~180 hr in the caudate and putamen respectively, and returning to the baseline (preinjection intensity level) after 361 hr on the caudate and 433 hr on the putamen side. In all of the cases, the tracts (corresponding to bundles of axons) of Mn^{2+} signal from the injection sites to the projection targets were clearly visible in the MR images (Figure 1D, green arrowhead; Figure 4B, red arrows).

MRI Visualization of Direct and Indirect Projections from the Striatum

Injection of $MnCl_2$ into the striatum (caudate and putamen) enabled MRI visualization of sets of efferent connections: direct projections from the striatum to the globus pallidus and substantia nigra and an indirect projection (transsynaptic) from the striatum to the thalamus via the globus pallidus and the substantia nigra.

Direct Projections from the Striatum

Anatomical MRI scans obtained within 24.5 hr (case 1), and 45 hr (case 2) after the injection of $MnCl_2$ into the caudate or putamen showed discrete regions of strong Mn^{2+} signal to increase in two areas that are known from previous anatomical studies to receive direct projections from the caudate and putamen: the globus pallidus and the substantia nigra (Figures 2–4).

Projections to the Globus Pallidus. Manganese signal was found in the globus pallidus in both the external and internal segments (GPe and GPi, respectively) after injection into the right caudate or the left putamen in case 1 (Figures 2A–2D, arrowheads). The pattern of Mn^{2+} signal observed in the MR images matched precisely the results of previous studies using conventional, tract-tracing methods realized in histological preparations (for a review, see Parent and Hazrati, 1995a). In this case, the distribution of Mn^{2+} signal in particular was wider and tended to be more prominent on the putamen injection side (Figures 2B–2D, left hemisphere). The signal

Table 2. Maximum Signal Changes in Percent (Time in Hours in Parenthesis)

	Case 1 (F00)		Case 2 (F97)		Case 3 (J00)		Case 4 (H00)
	Caudate	Putamen	Caudate	Putamen	Caudate	Putamen	Cortex
GPe	87.1% ± 5.8% (24.5 hr)	82.8% ± 4.7% (24.5 hr)	46.0% ± 6.8% (45 hr)	56.6% ± 13.2% (45 hr)	90.6% ± 16.6% (51.8 hr)	116.2% ± 8.8% (97.3 hr)	
GPi/VP**	75.3% ± 9.7% (24.5 hr)	61.5% ± 7.9% (24.5 hr)	44.0% ± 8.0% (42 hr)	47.6% ± 5.7% (45 hr)	63.2% ± 10.2% (97.3 hr)	74.6% ± 8.5 % (97.3 hr)	50.4% ± 8.0% (92.5 hr)
SNr	42.3% ± 6.6% (24.5 hr)	24.8% ± 3.3% (24.5 hr)	24.0% ± 4.6% (45 hr)	23.1% ± 4.5% (45 hr)	49.1% ± 4.2% (97.3 hr)	38.6% ± 6.0% (144.5 hr)	26.3% ± 3.1% (140.8 hr)
VA/VL			9.9% ± 4.2% (42 hr)	8.7% ± 3.2% (45 hr)	14.3% ± 2.0% (97.3 hr)	14.8% ± 3.5% (97.3 hr)	
Hb			11.4% ± 5.9% (45 hr)	13.5% ± 9.5% (39 hr)	28.3% ± 8.4% (144.5 hr)	42.2% ± 12.5% (191.8 hr)	
Corpus callosum							43.3% ± 2.1% (188 hr)
Ventral striatum							36.9% ± 3.2% (92.5 hr)
Cerebellum	–	–	–	–	–	–	–

GPe, globus pallidus external segment; GPi, globus pallidus internal segment; VP, ventral pallidum; SNr, substantia nigra pars reticulata; VA/VL, ventral anterior and ventral lateral thalamic nuclei; Hb, habenular thalamic nuclei.
** The VP region refers to case 4 (H00-cortex injection). The VP includes the region ventral to the anterior commissure and the rostral pole of the external pallidal segment (GPe) and the rostromedial internal pallidal segment (GPi) (Haber et al., 1993).

covered different mediolateral regions of the GPe and GPi after caudate and putamen injections (Figure 2D); the former resulted in signal distributed mostly in the dorsomedial portion (right hemisphere) and the latter in the ventrolateral or midportions of the GPe and GPi (left hemisphere). These projection sites (signal) remain segregated from one another throughout the entire extent of the globus pallidus (GPe and GPi). The differential distribution of Mn^{2+} signal in the GPe and GPi observed in the MR images was also confirmed histologically after WGA-HRP injection into the same locations in the caudate and putamen into which $MnCl_2$ had been injected (Figures 3A–3D). In the WGA-HRP-labeled sections, band-like fiber bundles distributed in both the GPe and GPi coincided well with the Mn^{2+} signal observed in the MR images (arrowheads in Figures 3C and 3D). This characteristic pattern consists of bundles of compact, anterogradely-labeled terminals aligned parallel to the medullary laminae on the putamen injection side and parallel to the internal capsule on the caudate injection side (Smith and Parent, 1986; Hazrati and Parent, 1992).

A similar spatial distribution of Mn^{2+} signal/WGA-HRP labeling in the globus pallidus was confirmed in case 2. In this case, the injections of $MnCl_2$/WGA-HRP into the striatum were reversed: left caudate and right putamen injections (Figures 1 and 3E–3F; Table 1). Here, the overall distribution of signal/labeling (projection foci) was similar to case 1, i.e., the projection foci were found in the dorsomedial portion of the GPe and GPi after caudate injection (left hemisphere) and in the ventrolateral or midportion of the GPe and GPi after putamen injection (right hemisphere) (Figures 3E and 3F).

We determined the positions and extents of Mn^{2+} signal and WGA-HRP labeling in the GPe and GPi in cases 1 and 2 in order to compare the specificity of the two tracers. The centers of the regions of significant Mn^{2+} signal increase in the MR images and the centers of the sites of WGA-HRP labeling in the histological sections were within 0.5 mm of each other, and they differed in size by an average of only 9%, indicating a very close correspondence in labeling for the two tracers.

The Mn^{2+} signal intensity measured in the GPe and GPi increased and had reached its maximum when the experiments were terminated at 24.5 hr for case 1 and 42–45 hr for case 2. The maximum percent signal change in the GPe and GPi in case 1 was 87.1% ± 5.8% and 75.3% ± 9.7%, respectively, on the caudate injection side and 82.8% ± 4.7% and 61.5% ± 7.9%, respectively, on the putamen injection side (Table 2). Although the signal in the GPe and GPi in case 1 appeared to be most prominent on the putamen injection side at 24.5 hr (Figures 2C–2D), the difference in maximum percent signal change between the caudate and putamen injection sides was not significant (Table 2). In case 2, the maximum percent signal change in the GPe and GPi appeared on the putamen injection side, rather than on the caudate injection side, at 42–45 hr postinjection (Table 2).

We estimated the transport rate for Mn^{2+} by computing the distance between the midpoints of the structures of interest and the injection sites and dividing this by the time required for the Mn^{2+} signal to reach a level of two standard deviations above the mean plus standard deviation of the baseline for cases 1 and 2. The grand mean for all three pathways (caudate or putamen to the GPe, Gpi, or SN) indicated that Mn^{2+} was transferred at a rate of 1.14 mm/hr, but this appeared to be dose dependent. A mean of 1.42 mm/hr was calculated for case 1 with injections of 0.5 and 1.0 μl in the caudate and putamen, respectively, whereas a mean of 0.64 mm/hr was observed for case 2 with injections of 0.1 and 0.15 μl.

Projections to the Substantia Nigra. The Mn^{2+} signal was distributed throughout the rostrocaudal extent of the substantia nigra (SN) after both the caudate and putamen injections (Figure 4; case 1). The intensity of the signal was stronger on the caudate injection side (Figure 4A, crosshairs) than on the putamen injection

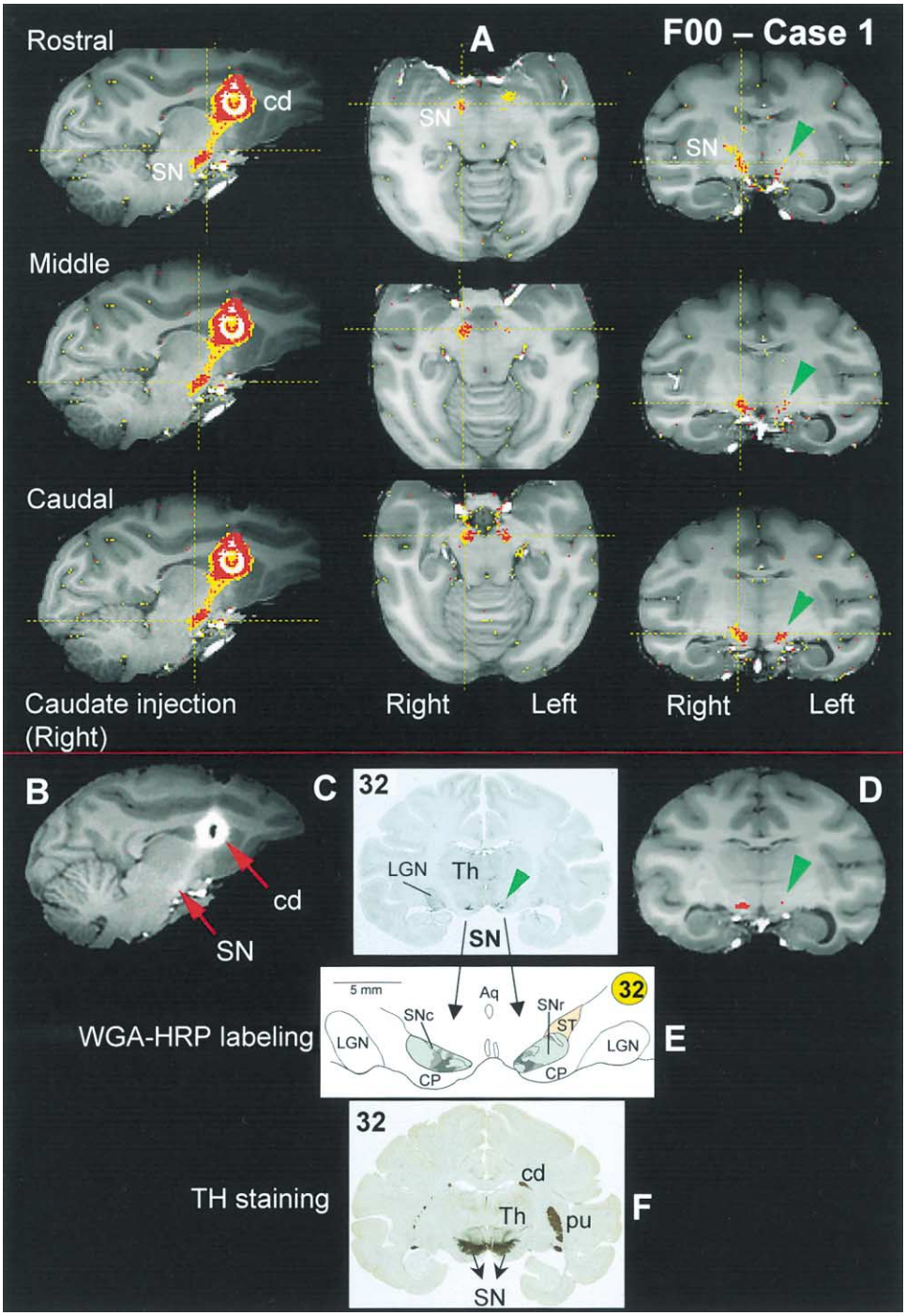

Figure 4. MRI Visualization of Mn^{2+} Signal in the Substantia Nigra (SN) 24.5 hr after Injection into the Caudate and Putamen in Case 1 (F00)

(A) Sagittal, horizontal, and coronal MR images from three different levels (rostral, middle, and caudal), illustrate the distribution of Mn^{2+} signal in the SN after right caudate (crosshairs) and left putamen (arrowheads) injections. The presence of signal is shown as statistical maps (unpaired t test comparing the baseline and 24.5 hr scans; $p < 0.02$) superimposed on the anatomical images. The yellow and red areas indicate regions of significant signal change, whereas the white at their centers indicates a region of no significant signal change. The first column in (A) shows only the signal from the caudate injection side (cd). The putamen injection site is not shown. The signal intensity is stronger on the caudate injection side (crosshairs) than on the putamen injection side (arrowheads).

(B) An MR image showing the raw Mn^{2+} signal at the caudate injection site and in the SN corresponding to the statistical maps in (A) (left column) is shown.

(C and D) Coronal histological section (#32) and the coronal MR image, respectively, show the WGA-HRP labeling (arrows) and Mn^{2+} signal (red shading) in SN. The coronal MR image shown in (D) was matched to the histological section in (C) by rotating and reslicing the volume at the appropriate AP extent using MEDx. The MR images in (A) are before reslicing. WGA-HRP injections were made at the same stereotaxic coordinates of the caudate and putamen as the $MnCl_2$ injections.

(E) Camera lucida drawing of the WGA-HRP labeled terminals (gray shaded regions) in the SN (green areas)is depicted. The darkest gray

side (Figure 4A, arrowheads). The signal in the SN was at its maximum (42.3% ± 6.6% on the caudate injection side and 24.8% ± 3.3% on the putamen injection side) at the termination of the experiment 24.5 hr postinjection (Table 2). Unlike the signal distribution in the globus pallidus, differences in the spatial distribution of signal originating from the caudate or putamen were not obvious in the SN (Figures 3C, 3E, and 4A). The signal tended to be concentrated in the medial part of the SN after both caudate and putamen injections (Figure 4A, coronal images). The rostrocaudal and mediolateral distribution of the Mn^{2+} signal in the SN was confirmed histologically after injection of WGA-HRP (Figures 4C and 4D). WGA-HRP-labeled terminals were found in the substantia nigra pars reticulata (SNr) (Smith and Parent, 1986; Parent and Hazrati, 1994), particularly in the medial portion of the SNr after rostral striatum injections (Figure 4E) (Hedreen and DeLong, 1991).

The overall distribution of the Mn^{2+} signal in the SN in case 2 (data not shown) was weaker than in case 1. In addition, the distribution of signal in the SN in case 2 did not show any bias toward the caudate or putamen injection side, in contrast to case 1 (Figure 4; Table 2). The maximum percent signal enhancement in the SN was observed in both cases at the termination of the MRI experiment after 24.5 or 45 hr.

The fact that the Mn^{2+} signal in all of the examined structures was at its maximum at the termination of scanning, as well as the presence of a weak but significant signal at 45 hr (case 2) in structures not known to receive a direct projection from the striatum (e.g., several thalamic nuclei; see Table 2: VA/VL and Hb) prompted two additional experiments in which the progress of the Mn^{2+} signal was followed over a longer period of time, up to 18 days.

Projections to the GP and SN: Long-Term Signal Changes. In the two cases (cases 1 and 2) described above, we examined the distribution of signal in the globus pallidus and the substantia nigra in the 24.5 and 45 hr period, after the injection of $MnCl_2$ into the striatum. In a third experiment (case 3), we studied the long-term (up to 432 hr/18 days) changes in the distribution of Mn^{2+} signal in these target areas after injection into the caudate and the putamen. In this case, we obtained a single scan every 2 days up to day 18 with 3-day intervals between the last three scans (ten scans in total, including a baseline scan made before the injection; Figure 5). For the sake of clarity, MR images from only five scans at different sampling times (4 hr and days 2, 6, 12, and 18) are shown in Figure 5A. The overall spatial distribution of signal in the globus pallidus and the SN was similar to that in the first two cases.

In general, both the spatial and temporal patterns of signal enhancement observed in the GPe and GPi in case 3 were very similar to those seen in cases 1 and 2. However, as expected, the Mn^{2+} signal in the GPe and GPi on both the caudate and putamen injection sides continued to increase beyond 45 hr and finally reached a maximum at 51.8 and 97.3 hr, respectively, on the caudate injection side and 97.3 hr on the putamen injection side (Table 2). The signal at the injection sites and in these two target areas (GPe and GPi) began to decrease by day 6 (144.5 hr), postinjection (Figures 5A and 5B; see also supplemental movies S1 and S2 online at http://www.neuron.org/cgi/content/full/34/5/685/DC1). None of the cases showed signal increase in the cerebellum (Table 2; see Experimental Procedures).

In the substantia nigra, a large signal increase was observed on the caudate injection side after 2 days (Figures 5A and 5B). The signal continued to increase, reaching a maximum at day 4 (97.3 hr). The maximum percent signal change on the putamen injection side was reached at day 6 (144.5 hr) (Table 2). As in case 1 (see Figure 4), the maximum percent signal change in the SN was greater on the caudate injection side than on the putamen injection side. The inverse was true for the globus pallidus in this case and in case 2 as well (Figure 5B; Table 2).

Indirect Projections from the Striatum

In addition to the globus pallidus and substantia nigra (SN), several thalamic nuclei (the ventral anterior and ventral lateral nuclei [VA/VL] and the Habenular nucleus [Hb]) showed a strong signal increase after $MnCl_2$ injection into the caudate or putamen in cases 2 and 3 (Figure 6; Table 2). The aforementioned thalamic nuclei were defined in the MR images on the basis of cytoarchitectonic maps obtained from publications of previous studies in the macaque monkey (Ilinsky et al., 1985; Smith and Parent, 1986; Ilinsky and Kultas-Ilinsky, 1987; Sidibé et al., 1997). These thalamic nuclei are known to receive direct projections from the internal segment of the globus pallidus (GPi), and/or the SN (Nauta and Mehler, 1966; Devito and Anderson, 1982; Sidibé et al., 1997; Parent et al., 2001), but not from the caudate or the putamen. In the Hb, the distribution of signal was discrete and prominent and tended to be located in the lateral part of the nucleus (Figures 6A and 6B). The intensity of the signal in Hb was sufficient to clearly distinguish this nucleus in the MR images of successive scans (Figure 6B). In contrast, the distribution of signal in the VA/VL was more diffuse and less prominent (Figure 6C). In the case of the VA/VL, the borders of which were particularly difficult to see in the MRI scans, we defined this region by using the correspondence between identifiable anatomical landmarks (e.g., the internal capsule and the head of the caudate nucleus) and maps of statistically significant signal change, which we derived by comparing late time point scans with the baseline scan (see Figure 6D). The signal intensity measured in the Hb reached a maximum at 39 and 45 hr in case 2 and at

regions indicate the highest density of labeled terminals. This drawing was made from the histological section (#32) shown in (C). The WGA-HRP labeled terminals were found mainly in the medial part of the substantia nigra pars reticulata (SNr).

(F) The coronal histological section stained for tyrosine hydroxylase (TH), showing the anatomical location of the SN. This histology section matches the MR image shown in (D). The histological sections shown in (C) and (F) are adjacent sections.

Abbreviations: Aq, aqueduct; cd, caudate; CP, cerebral peduncle; LGN, lateral geniculate nucleus; pu, putamen; SNc, substantia nigra pars compacta; ST; subthalamic nucleus; and Th, thalamus.

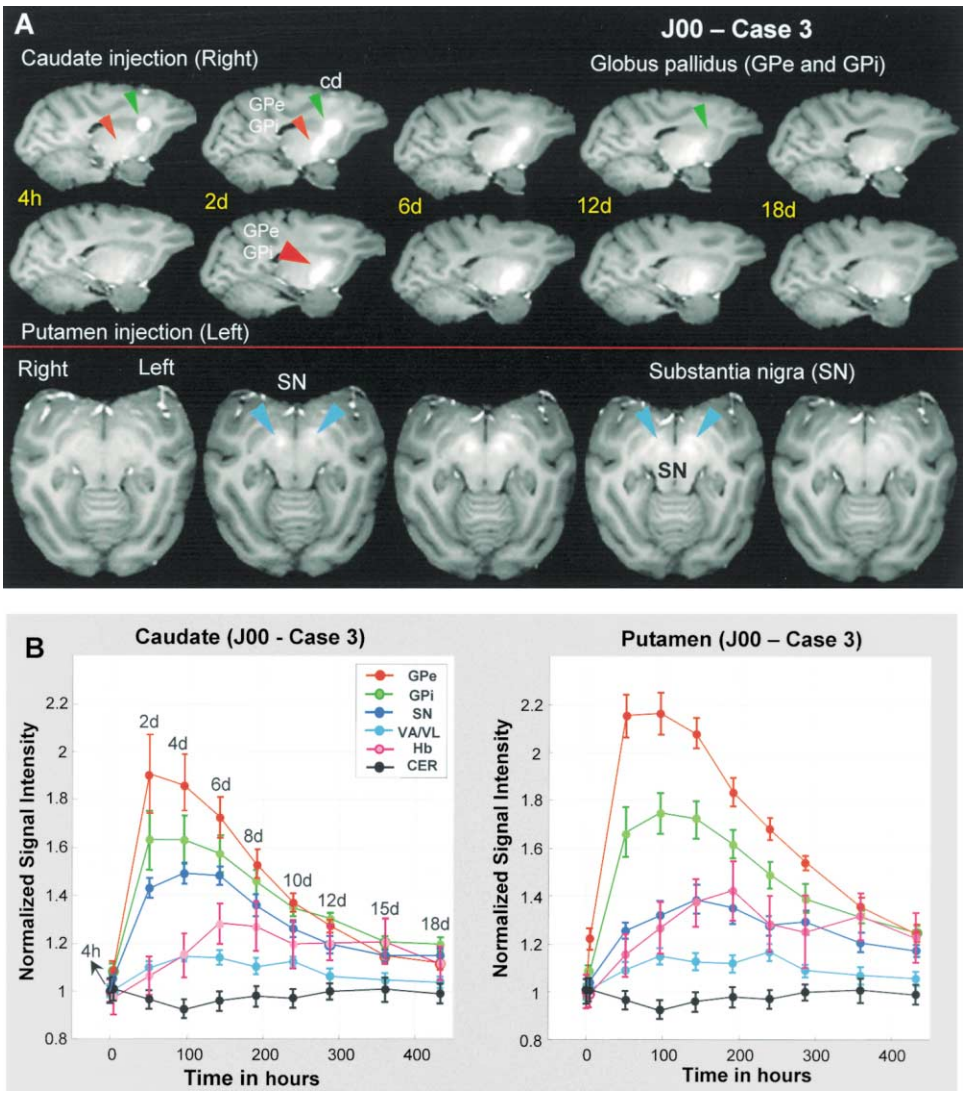

Figure 5. MRI-Detected Mn^{2+} Signal Changes over Long Time Periods (4 hr–18 days) in the Globus Pallidus (GPe and GPi) and Substantia Nigra (SN) after $MnCl_2$ Injection into the Caudate and Putamen in case 3 (J00).

(A) Here, a single scan was obtained every 2 days up to day 18, with 3-day intervals between the last three scans (ten scans total, including one prior to the injection). For clarity, MR images from only five scans at different time points (4 hr and days 2, 6, 12, and 18) are shown. In row 1, sagittal MR images from the right hemisphere showing the extents of the $MnCl_2$ injection site in the head of the caudate nucleus (green arrowheads) and the distribution of Mn^{2+} signal in the GPe and GPi (red arrowheads) are shown. In row 2, sagittal MR images from the left hemisphere illustrating the distribution of Mn^{2+} signal in the GPe and GPi after the putamen injection are shown. No putamen injection site is visible at this mediolateral extent. Note the strong signal increase in the GPe and GPi on days 2 and 6 after the $MnCl_2$ injection. Also, note the signal intensity decrease at the caudate injection site (green arrowheads; row 1) on days 6 and 12 after the injection. In row 3, horizontal MR slices showing Mn^{2+} labeling in the SN (blue arrowheads) are shown. Note the strong signal increase in the SN on days 2 and 6 (for other labeling conventions see Figure 2).

(B) Time course of MRI signal-changes in the globus pallidus (GPe and GPi), substantia nigra (SN), ventral anterior and ventral lateral thalamic nuclei (VA/VL), and habenular thalamic nuclei (Hb) after $MnCl_2$ injections into the caudate and putamen (J00, case 3). As a control, the signal intensity in the cerebellum (CER) at different time points is indicated. The ordinate shows the ratio-normalized signal intensities for each region (i.e., each region normalized to its initial intensity). Note that the signal intensity in the SN is stronger on the caudate injection side than on the putamen injection side between days 2 and 6 postinjection. The inverse is true for the globus pallidus. Bars show 1 SD.

192 and 145 hr in case 3 (Figure 5B; Table 2) after putamen and caudate injections, respectively. The signal intensity measured in VA/VL reached a maximum at 45 and 42 hr in case 2 and at 97 hr in case 3 after putamen and caudate injections, respectively (Figure 5B; Table 2). The Mn^{2+} signal in the VA/VL was weaker than in the Hb. At its maximum, the percent signal enhancement in the VA/VL and the Hb, respectively, was 14.3% $\pm$ 2.0% and 28.3% $\pm$ 8.4% on the caudate injection side, and 14.8% $\pm$ 3.5% and 42.2% $\pm$ 12.5% on the putamen

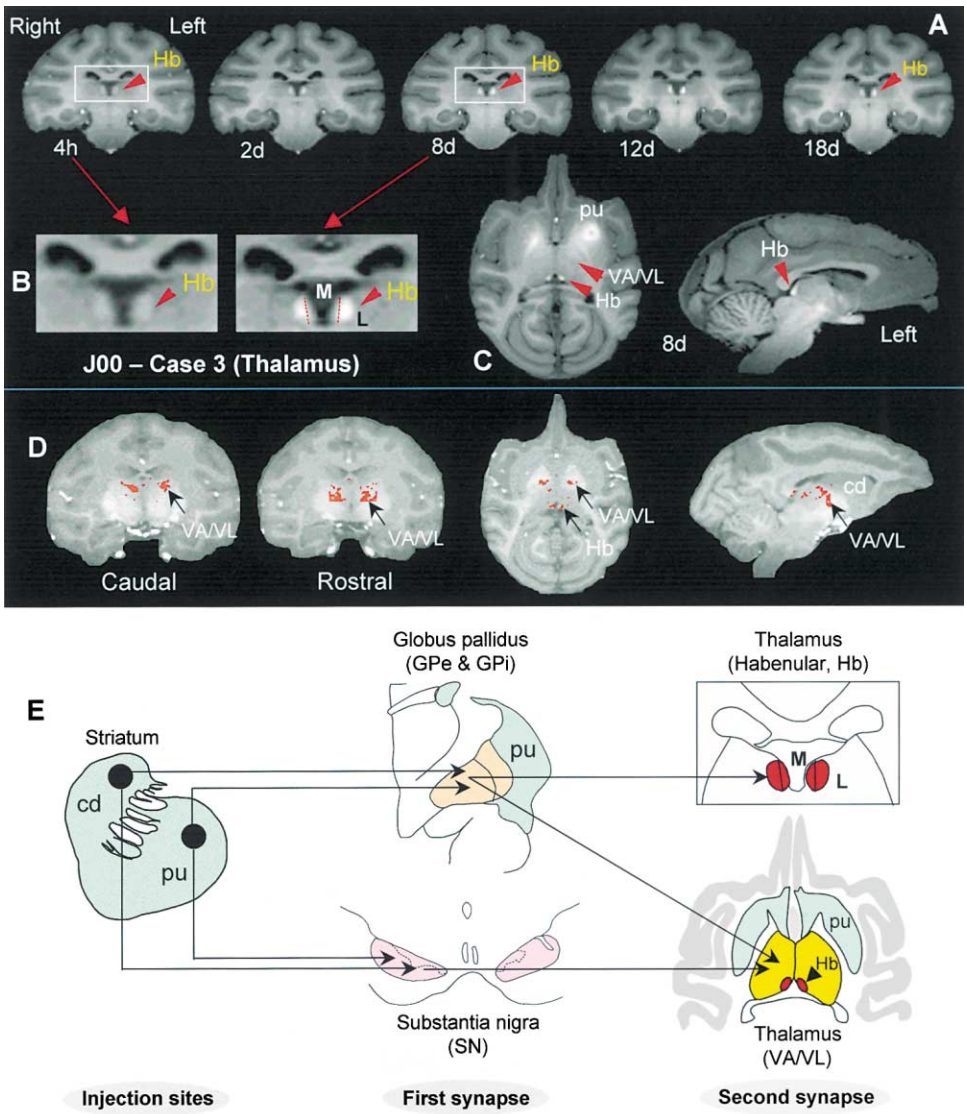

Figure 6. Mn^{2+} Signal Changes in Thalamic Nuclei over Long Time Periods (4 hr–18 days) after $MnCl_2$ Injection into the Right Caudate and Left Putamen in Case 3 (J00)

(A) Coronal MR images from five different scans (4 hr and days 2, 8, 12, and 18; see Figure 5) show the Mn^{2+} signal in the habenular thalamic nuclei (Hb, bright discrete regions; arrowheads).

(B) Enlargement of the Hb from the rectangular area indicated in the 4 hr and day 8 scans is shown. Note the difference in Mn^{2+} signal intensity in the Hb between the 4 hr and day 8 scans. Abbreviations: M, medial; L, lateral

(C) The horizontal and sagittal MR images from one of the scans (day 8) showing Mn^{2+} in the Hb and subregions of the other thalamic nuclei (corresponding to the ventral anterior and ventral lateral thalamic nuclei; VA/VL). The histology is not available in this case. We identified thalamic nuclei in the MR images on the basis of cytoarchitectonic maps from previous studies in the macaque monkey (see text).

(D) Difference images derived from scans one (before the injection) and three (52 hr postinjection) show voxels with a signal increase greater than 1 SD from the mean signal intensity of the same region in scan one. The red areas indicate the Mn^{2+} signal in the thalamic nuclei (VA/VL and Hb). The signal in other regions (cd, pu, and GP) is masked so that only the thalamic regions are visible. The signal in the thalamus is superimposed on sagittal, horizontal, and coronal anatomical MR images. The coronal sections (caudal and rostral) are 1.5 mm apart.

(E) Schematic representation of the direct projections from the striatum (cd and pu; green shading) to the globus pallidus (GPe and Gpi; orange shading) and substantia nigra (SN; pink shading), and the indirect (transsynaptic) projections from the striatum to thalamus (part of the yellow shading and red shading) via the GPi and SN.

injection side (Table 2, case 3). We could not find any signal increase in these areas at 24.5 hr (termination of the experiment) in case 1.

Although significant signal could be identified statistically in other subregions of the thalamus (Figure 6D), the resolution and contrast of the anatomical scans was not sufficient to define other nuclei such as the centromedian nucleus-parafascicular complex and mediodorsal thalamic nucleus, which are known to receive projections from the GPi or SN (Devito and Anderson,

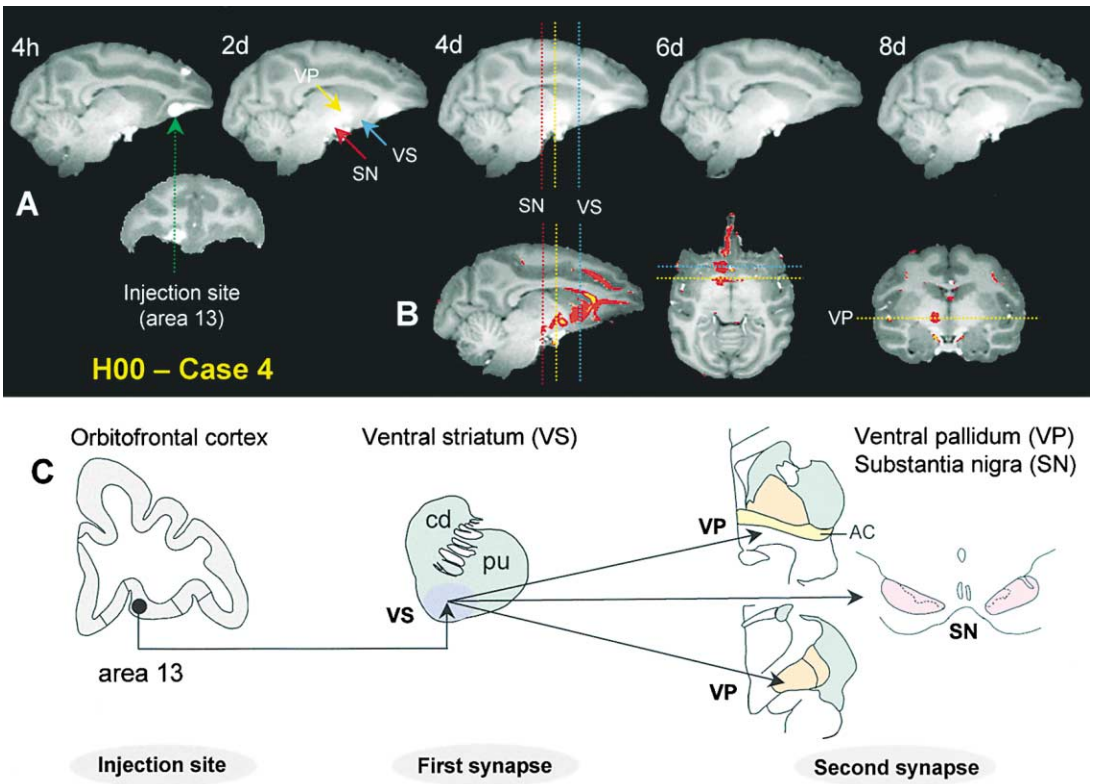

Figure 7. Mn^{2+} Signal Changes in the Ventral Striatum (VS), Ventral Pallidum (VP), and the Substantia Nigra (SN) over Long Time Periods (4 hr–8 days) after $MnCl_2$ Injection into the Right Orbitofrontal Cortex in Case 4 (H00)

In this case, a single scan was obtained every other day up to day 8 (six scans in total, including one before the injection).

(A) Sagittal MR images from five different scans (4 hr and days 2, 4, 6, and 8) show the $MnCl_2$ injection site in the orbitofrontal cortex (green arrow; also dashed line in coronal image) and the distribution of Mn^{2+} signal in the VS (blue arrow/dashed line), VP (yellow arrow/dashed line), and SN (red arrow/dashed line).

(B) Statistical map (colored region, unpaired t test between the mean of scans of days 4, 6, and 8 and 4 hr with a single threshold [$p < 0.02$]) superimposed on sagittal, horizontal, and coronal anatomical MR images. The dashed lines indicate the AP (anteroposterior) level of the VS (blue), VP (yellow), and SN (red).

(C) Schematic representation showing the direct projection from the orbitofrontal cortex to the VS (gray shading) and the indirect (transsynaptic) projections from the orbitofrontal cortex to the VP and SN via the VS is depicted. The VP includes the region (white) ventral to the anterior commissure (AC; yellow shading) and rostral pole of the external pallidal segment and the rostromedial internal pallidal segment (GPe and GPi, respectively; orange shading) (Haber et al., 1993).

1982; Ilinsky et al., 1985; Sidibé et al., 1997). We also found no clear signal in the anterior part of the prefrontal cortex, including the principal sulcus and orbital cortex, both being areas known to receive input from the SN via specific thalamic nuclei (Ilinsky et al., 1985).

Direct and Indirect Projections from the Orbitofrontal Cortex Visualized Using MRI

The visualization of Mn^{2+} signal after $MnCl_2$ injection into area 13 of the orbitofrontal cortex (case 4) illustrated the well-known direct projection from the cortex to ventral striatum and the indirect projection (transsynaptic) from the cortex to the ventral pallidum and substantia nigra via the ventral striatum.

We obtained anatomical and angiography scans every 2 days up to day 8 (five scans in total; Figures 7 and 8) to examine long-term changes in the distribution of Mn^{2+} signal in the basal ganglia. Significant signal enhancement was found in the ventral part of the striatum (ventral striatum [VS]) starting 2 days after the injection into the orbitofrontal cortex (Figures 7A and 7B). The VS includes both the nucleus accumbens and the ventral parts of the caudate and the putamen and receives a direct projection from area 13 of the orbitofrontal cortex (Haber et al., 1995; Ferry et al., 2000). The distribution of signal was rather diffuse in the VS. The greatest signal increase was observed in the ventral pallidum (VP), starting at 2 days postinjection and reaching maximum at 4 days (around 94 hr) postinjection (Figures 7 and 8; Table 2). The VP includes a region ventral to the anterior commissure and the rostral pole of the external pallidal segment (GPe) and the rostromedial internal pallidal segment (GPi) (Haber et al., 1993). A significant enhancement was also seen in the SN, starting at day 2 and reaching a maximum at day 6 (around 142 hr) postinjection (Figures 7 and 8). These areas (VP and SN) receive no direct projection from area 13 of the orbitofrontal cortex, but studies with conventional tracers have demonstrated

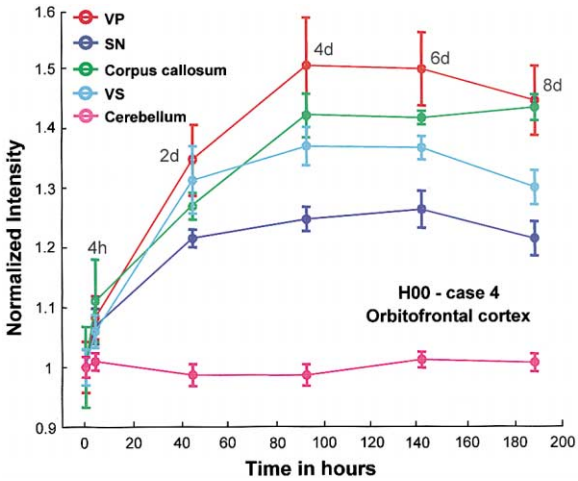

Figure 8. Time Course of MRI Signal Changes (4 hr–8 days) in the Ventral Striatum (VS), Ventral Pallidum (VP), Substantia Nigra (SN), and Corpus Callosum after $MnCl_2$ Injections into the Orbitofrontal Cortex (H00–case 4).

As a control, the signal intensity in the cerebellum at different time points is indicated. The intensity values were normalized as described in Figure 5B. The bars show standard deviations.

that they receive projections from the orbitofrontal cortex via the ventral striatum (Haber et al., 1993, 1995, 2000) (Figure 7C).

Further Observations from the Long-Term Studies

The neurotoxic effects of excessive chronic or acute doses of manganese are very well known and have been extensively studied. For example, several studies carried out in rats have investigated the mechanisms of manganese sequestration, transport, and toxicity in the brain (London et al., 1989; Aschner and Aschner, 1991; Sloot and Gramsbergen, 1994). Efforts to develop heavy-metal, ion-based contrast-enhancement agents, including manganese, have in turn awakened renewed interest in determining and understanding their potential side effects. The aim of this study was not to address issues of manganese neurotoxicity, but the experiments of cases 3 and 4 allowed us to observe not only tracer progress over long periods of time, but also the behavior of the animals. Case 3 and 4 were scanned again after a recovery period (2–3 weeks) following termination of the experiments (day 18 in case 3 and day 8 in case 4). No significant Mn^{2+} signal could be found in any of the regions of interest (ROIs) used for data analysis during the experiments in those cases. Furthermore, we expected that animals suffering from manganese toxicity in the injected regions (striatum) or regions exhibiting increased Mn^{2+} signal due to direct projections from an injected region (such as striatum to globus pallidus and substantia nigra or the orbitofrontal cortex to the ventral striatum) would display symptoms associated with massive cell death in these regions (in particular, motor-related symptoms). However, neither of the animals showed any motor deficits or coordination problems whatsoever.

Discussion

The present study provides a detailed account of a highly selective method for MRI visualization of neuronal pathways in the macaque monkey, particularly, the efferent projections of the striatum (striatofugal projections; cases 1, 2, and 3) using the MRI-visible contrast agent $MnCl_2$. Direct projections from the striatum were confirmed histologically in the same animals by injecting WGA-HRP at the same sites where $MnCl_2$ had been injected. The size and location of the projection foci in the striatal targets were comparable to those found in both the MR and histology images. This opens up the possibility of using manganese as an in vivo standard MRI-visible tract tracer in primates. Furthermore, our results conclusively demonstrate the transsynaptic transport of Mn^{2+} in the primate. Pautler et al. (1998) suggested that Mn^{2+} must have traversed a synapse to explain the enhancements detected in the olfactory cortex of the mouse following the application of manganese chloride to its olfactory epithelium. Watanabe and colleagues (2001), on the other hand, reported that the signal enhancement they observed in their rat study was confined to regions known to receive direct projections from the retina and concluded that it did not constitute evidence for transsynaptic crossing of Mn^{2+}. Here, we present data shortly following the injections, demonstrating the absence of Mn^{2+} signal in structures other than those injected (Figure 5A, row 1, 4 hr scan). By injecting WGA-HRP at the same sites as $MnCl_2$, we also confirmed for each animal the absence of a direct connection from the injection sites to several brain structures (e.g., thalamic nuclei) that show significant signal enhancement at considerably later time points. In other words, we were able to track significant signal changes in brain structures receiving no direct projections from the injected structures. The transsynaptic transport of Mn^{2+} was observed after 45 hr in case 2 and could be confirmed in two long-term studies (cases 3 and 4) in which we followed the progress of the Mn^{2+} signal through its maximum until it began to decline in both direct and indirect projection targets.

Our findings demonstrate that the injection of $MnCl_2$ into the caudate and putamen leads to the distinct spatial localization of Mn^{2+} signal (projection foci) in the external and internal segments of the globus pallidus. The projection foci were localized in the dorsomedial portion of the globus pallidus after caudate injection and in the ventrolateral or midportion of the globus pallidus after putamen injection (Figures 2 and 3). These projection foci remain segregated from one another throughout the entire extent of the globus pallidus. In addition, the projection foci tended to be more distinct on the putamen injection side than on the caudate injection side. The pattern of topographical organization of striatopallidal projections observed with MRI after $MnCl_2$ injection was similar to that shown in previous studies using standard anatomical tracing methods (Johnson and Rosvold, 1971; Smith and Parent, 1986; Hedreen and DeLong, 1991; Hazrati and Parent, 1992; Parent and Hazrati, 1995a).

In contrast, the spatial localization of Mn^{2+} signal after the injection of $MnCl_2$ into the caudate and putamen was less distinct in the substantia nigra. The Mn^{2+} signal

was considerably stronger on the caudate injection side than on the putamen injection side. The organizational pattern of striatonigral projections revealed by Mn^{2+} with MRI was comparable to that found in previous anatomical tracing studies in monkeys (Smith and Parent, 1986; Parent and Hazrati, 1994, 1995a). Using standard anterograde tracing methods, Parent and Hazrati (1994) found that the putaminonigral fibers are less abundant than the caudatonigral fibers and that they form terminal plexuses that are smaller and more loosely organized than those formed by caudatonigral fibers, but that the arborization pattern of both types of striatonigral fibers is strikingly similar. Thus, in the present study, the less intense signal observed on the putamen injection side might be due to fewer terminal plexuses in projection foci within the substantia nigra.

The spatial distribution of Mn^{2+} signal observed in the globus pallidus and substantia nigra following injection in the caudate and putamen was confirmed histologically in the same animal after WGA-HRP injection at the same sites. We found that the Mn^{2+} signal (projection foci) in both the globus pallidus and substantia nigra coincided well with that of the WGA-HRP labeling observed in the histology (see Figures 3 and 4). The size and location of the projection foci in both of the targets receiving a direct projection were comparable in both the MRI and histological images. Our WGA-HRP results are in very good agreement with other studies examining striatopallidal and striatonigral projections (Johnson and Rosvold, 1971; Smith and Parent, 1986; Hedreen and DeLong, 1991; Hazrati and Parent, 1992; Parent and Hazrati, 1994, 1995a).

The unique finding of the present study was the selective distribution of Mn^{2+} signal in areas not receiving direct projections from the injection sites. In addition to the signal intensity increases observed in the globus pallidus and the SN, we also found significant increases in several thalamic nuclei not known to receive direct projections from the caudate or putamen: (1) the ventral anterior and ventral lateral nuclei (VA/VL) and (2) the habenular nucleus (Hb). The distribution of signal in the Hb was discrete and more prominent than in the VA/VL complex (Figure 6). It is known that the VA/VL receives projections from the internal segment of the globus pallidus (GPi) and the substantia nigra pars reticulata (SNr), whereas the Hb, in particular the lateral Hb, is known to receive projections primarily from the GPi (Nauta and Mehler, 1966; Devito and Anderson, 1982; Ilinsky et al., 1985; Hazrati and Parent, 1991; Parent and Hazrati, 1995a; Sidibé et al., 1997; Parent et al., 2001). Moreover, a recent single-axon study showed that the pallidohabenular projection is a highly prominent component of the pallidal outflow and stands out as a densely innervated pallidal target (Parent et al., 2001). The present findings show conclusively that Mn^{2+} is transported transsynaptically from the striatum to these thalamic nuclei via the globus pallidus and the substantia nigra (Figure 6E).

Several lines of evidence obtained in a number of species suggest that unlike striatofugal connections, the efferent projection from the globus pallidus (pallidofugal system) is, at least in part, bilaterally distributed (Parent et al., 1999, 2001). Theoretically, both ipsilateral and contralateral GP projections could have contributed to the signal observed in the thalamic nuclei. However, this is not likely to have been the case because the density of the termination was significantly lower contralaterally than ipsilaterally (Devito and Anderson, 1982; Parent et al., 2001). A similar interpretation can be applied to the projections of the substantia nigra. The SN receives direct and indirect projections from multiple sources: (1) a direct projection from the striatum to the SNr and (2) an indirect projection from the striatum to the SNr via two synapses, the outer segment of the globus pallidus (GPe) and the subthalamic nucleus (ST) (Alexander et al., 1990; Parent and Hazrati, 1995b). Thus, both direct and indirect projections might have contributed to signal observed in SN. However, anatomical evidence has shown that the indirect projections (Striatum-GPe-ST-SNr) are weak in primates (for a review, see Parent and Hazrati, 1995b).

The advantage of the present technique is the ability to visualize both direct and indirect (i.e., transsynaptic) projections using MRI in the same animal. This sets it apart from standard tracing techniques, which require fixed tissue for the visualization of labeled terminals and neurons and, in most cases, only provide information about direct projections. A number of studies using radioactively-labeled substances, such as proline or fucose (Wiesel et al., 1974), or viruses, particularly, the herpes simplex virus type 1 (HSV1) (for review see Kuypers and Ugolini, 1990) to investigate the retino-thalamo-cortical circuit (see Wiesel et al., 1974) or circuits that link the basal ganglia and/or the cerebellum with the cerebral cortex (Middleton and Strick, 1994, 1996; Hoover and Strick, 1999) demonstrated both anterograde (proline and fucose) and retrograde (HSV1) transneuronal transport. These methods, however, also require fixation of the tissue before the distribution of label can be visualized.

In summary, our study confirms and extends the work of Pautler and colleagues (1998), demonstrating conclusively the feasibility of using manganese as an MRI-visible, anterograde, highly selective transsynaptic neuronal tract tracer in both cortical and subcortical structures in the primate. The selectivity (anterograde transport) of this tracer is also convincingly shown recently in the mice olfactory pathway (Pautler and Koretsky, 2002). In the present study, the distribution of the MRI-visible Mn^{2+} signal closely matched the WGA-HRP labeling in the same animal, providing evidence for specificity and resolution comparable to that of conventional tract tracing methods. Furthermore, the fact that the Mn^{2+} signal eventually returned to baseline in all labeled regions and that no signs of manganese toxicity could be observed in the two long-term studies further enhances the appeal of Mn^{2+} for use as a standard MRI tract tracer. These three characteristics (good localization, nontoxicity at the dosages used, and eventual return to baseline), in addition to its MRI-visibility, make Mn^{2+} ideal for a number of types of studies that would otherwise be difficult if not impossible to carry out in the living brain. For instance, combined behavioral and electrophysiological experiments guided by Mn^{2+} connectivity maps obtained in such MRI tract-tracing experiments offer a unique opportunity to study distributed neural networks on an individual-animal basis. Comparing such anatomical maps with the activation maps obtained in functional imaging experiments can, in addition, provide useful

insights into the functional role of the observed connections in the context of different sensory stimulation conditions or behaviors. Studies with paramagnetic tracers can also be of invaluable help in the development and optimization of other noninvasive tract-tracing techniques such as diffusion tensor imaging. They can also provide important information regarding nerve regeneration after injury in the peripheral nervous system. Last, but not least, the technique presented here provides an exquisite tool for the study of plasticity and reorganization of the brain during development or after brain injury.

Experimental Procedures

Four rhesus monkeys weighing between 4.8 and 10 kg were used. All studies were approved by the local authorities (Regierungspraesidium) and were in full compliance with the guidelines of the European community (EUVD 86/609/EEC) for the care and use of the laboratory animals.

Surgery and Tracer Injection

The tracer ($MnCl_2$ or WGA-HRP) was stereotaxically injected under general anesthesia using aseptic techniques. After premedication with Robinul (0.01 mg/kg, i.m.) and ketamine (15 mg/kg, i.m.), anesthesia was induced by the intravenous injections of fentanyl (0.003 mg/kg), thiopental (5 mg/kg), and succinylcholine chloride (3 mg/kg). Following the intubation of the trachea, the lungs were ventilated using a Servo Ventilator 900 C (Siemens, Germany), maintaining an end-tidal CO_2 of 35 mm Hg and oxygen saturation over 95%. Balanced anesthesia was maintained with end-tidal 1%–1.6% isoflurane in air and fentanyl (0.003 mg/kg/hr). The temperature, ECG, NIBP, CO_2, and SpO_2 were monitored throughout surgery (Logothetis et al., 1999).

Manganese chloride ($MnCl_2$; Sigma-Aldrich) was injected into the rostral aspect of the head of the right caudate nucleus and left putamen in each of two animals (cases 1 and 3; Table 1), and vice versa in one animal (case 2). All of the injections were made bilaterally in the rostral part of the striatum because striatofugal connections are unilateral (Nauta and Mehler, 1966). In a fourth monkey, we injected $MnCl_2$ into the right orbitofrontal cortex, a region corresponding to cytoarchitectonic area 13 (Walker, 1940; Barbas and Pandya, 1989; Carmichael and Price, 1994) to study a set of inputs (corticostriatal) to striatum (case 4, Table 1). In cases 1 and 2, the $MnCl_2$ (0.8M) was dissolved in a physiological saline solution (0.9% NaCl in H_2O), while in cases 3 and 4 heavy (deuterium) water (D_2O) was used in place of H_2O to eliminate the contribution of additional hydrogen at the injection site to the signal.

The $MnCl_2$ injection was made by pressure using 0.5 and 1.0 μl Hamilton syringes fitted with 32 and 26 G needles, respectively. The tip of the needle was advanced into the caudate or putamen through a bur hole (7 mm in diameter) made in the right or left frontal region and then $MnCl_2$ (0.1 to 1.0 μl; for comparison, one voxel is equal to 0.125 μl) was injected into the head of the caudate nucleus or putamen over 10 to 25 min (Table 1; cases 1–3). The syringe was left in the brain for 15 to 30 min after the injection to minimize leakage of the tracer, and then retracted in 3 steps to avoid leakage of the tracer along the needle track. First, the syringe was pulled back 1 mm and left for several minutes, then 0.5 mm and left for another couple of minutes, and finally withdrawn slowly and smoothly from that point up to the pial surface. For the orbitofrontal injection (case 4), the tip of the needle was inserted through the bur hole made over the dorsal part of the right prefrontal cortex and then 0.1 μl of $MnCl_2$ was injected into area 13 (in the medial orbital sulcus).

Two of the animals (cases 1 and 2) also received a focal injection of the antero- and retrograde tracer WGA-HRP (5%, Toyobo, Japan) at the same stereotaxic coordinates as the caudate and putamen $MnCl_2$ injections following MRI scanning (24.5 hr in case 1 and 45 hr in case 2 after $MnCl_2$ injection). The injection parameters and the amount of tracer injected was the same as for the $MnCl_2$ injections, except for case 1, where the injected volume of WGA-HRP was less than that of $MnCl_2$ (Table 1). Cases 1 and 2 were perfused 2 days following the injection of WGA-HRP, and the brains were processed for histology. Cases 3 and 4 were survival experiments for which no histology was done. These two cases were observed for the manifestation of any toxic side effects of these doses of $MnCl_2$ (Table 1), but neither of the animals exhibited any of the well-known neurological symptoms associated with manganese toxicity (so-called extrapyramidal disorders involving Parkinson's-like symptoms) (Barbeau, 1984; Newland et al., 1989).

Histology and Tissue Processing

2 days after the WGA-HRP injection, cases 1 and 2 received a lethal dose of sodium pentobarbital (120 mg/kg) and were perfused transcardially with 2 liters of 0.9% warm heparinized saline, followed by 1 liter of cold 1% paraformaldehyde in 0.1 M phosphate buffer (pH 7.2–7.4), then 4 liters of 4% paraformaldehyde in 0.1M phosphate buffer, 1–2 liters of 10% sucrose, and finally by 20% and 30% sucrose in 0.1 M phosphate buffer (Saleem and Tanaka, 1996). The flow rate of the fixative solution was adjusted so that the perfusion with paraformaldehyde took 45–60 min. The brain was immediately removed from the skull, blocked, photographed, and then placed in 30% buffered sucrose at 4°C until it sank. 50 μm-thick frozen sections (both hemispheres together) were cut serially in the coronal plane . Every fifth section (250 μm interval) was processed for WGA-HRP histochemistry. The adjacent series of sections was stained for Nissl and tyrosine hydroxylase (TH) to determine the areal borders of the caudate, putamen, globus pallidus external segment (GPe), globus pallidus internal segment (GPi), substantia nigra (SN), and the thalamus. The HRP reaction was performed using the modified tetramethyl benzidine method (Gibson et al., 1984).

Histological Data Analysis

The WGA-HRP-stained histology sections were observed with a light microscope under bright- and dark-field illumination. The global distributions of WGA-HRP-labeled terminals in the globus pallidus and substantia nigra were charted using a Nikon light microscope equipped with a camera lucida. These drawings were lined up against the corresponding histology sections to show the spatial extent of labeling in the globus pallidus or the substantia nigra (see Figure 4). In both the WGA-HRP-injected cases (cases 1 and 2), MR images were matched to the corresponding histology sections by rotating and reslicing the volume at the appropriate AP extent using MEDx program.

MRI Data Collection and Analysis

Measurements were made in a vertical 4.7 T (200 MHz) scanner with a 40 cm diameter bore (Biospec 47/40v, Bruker Medical, Ettlingen, Germany). The gradient of 26 cm inner diameter was actively shielded and water-cooled, with a strength of 50 mT/m at 180 μs rise time (Bruker, B-GA 26). Cases 1 and 2 were imaged using a 120 mm wide, custom-made linear homogeneous volume (saddle) coil for both transmit and receive (Logothetis et al., 2002). A linear birdcage-type resonator with an inner-diameter of 198 mm (Bruker Medical, Ettlingen, Germany) was used for cases 3 and 4. The larger birdcage resonator delivered superior homogeneity over the entire brain volume and was, therefore, chosen for the long-term studies (cases 3 and 4; Figures 5 and 7). It also allowed room for liquid-filled markers extending from the ears, as well as a spherical, water-filled calibration phantom placed beside the head.

Shimming was performed with the FASTMAP shim algorithm (Gruetter, 1993), which uses projections through a predefined volume to measure B_0 inhomogeneity and applies first and second order corrections. In all cases, the B_0 inhomogeneity after corrections along each of six projections through a $25^3 mm^3$ cubic volume inside the brain was less than 8 Hz and, in most cases, less than 6 Hz.

We used a modified driven equilibrium with Fourier transform (MDEFT) method (Lee et al., 1995) to obtain T1 weighted anatomical images. The imaging sequence uses adiabatic spin preparation with 90° and 180° pulses and a segmented gradient-echo acquisition (Tau = 800 ms, TR = 21 ms, TE = 4 ms). For cases 1 and 2 (F00 and F97, respectively), we collected four segments and four averages of a $256^2 \times 128$ matrix in 2 hr:47 min per image, using a field of view of $128^2 \times 64$ mm. For cases 3 and 4 (J00 and H00, respectively) we

collected three averages and eight segments for an image acquisition time of 2 hr:8 min to obtain $256^2 \times 140$ matrices at FOV $128^2 \times 70$ mm. All scans achieved an isotropic voxel resolution of 0.5^3 mm^3.

We used a gradient-echo time-of-flight (GE TOF, TR = 22 ms, TE = 9 ms) method (Wehrli et al., 1986; Gullberg et al., 1987) to obtain angiographies of arterial blood flow in the brain. The angiography scans were obtained with the same image resolution as the anatomy scans. Baseline (reference) anatomy scans were obtained for cases 3 and 4 preceding the tracer injections. For cases 1 and 2, the first scan immediately following the injection was used as the baseline.

Each scan was normalized (ratio normalization) by dividing each pixel's intensity value by the mean intensity of a tracer-free region in the scan and multiplying the result by 5000. This procedure is immune to considerable differences in the average intensity that can arise during data collection, such as differences in receiver gain or in the quality factor, Q, of coils. In cases 1 and 2, we normalized the intensities in the anatomy time-series images using the signal intensity in muscle tissue as a reference and verified the normalization in the cerebellum. The cerebellum was chosen to confirm the normalization because we were quite certain we would not find any signal there within the durations of the experiments, based on the known connectivity (Zemanick et al., 1991; Middleton and Strick, 1994). For cases 3 and 4, we placed a sphere filled with T1 reduced water (10 mM Cu_2SO_4) at the side of the animal's head and used the water signal intensity for normalization. The normalization was again verified in the cerebellum. Using liquid-filled markers in the ears, we manually registered the images in the Horsley-Clark stereotaxic coordinate system (Horsley and Clark, 1908), whose horizontal reference plane, known as the Frankfurt zero, is determined by the infraorbital ridge and the middle of interaural line connecting the external auditory meati. The Horsley-Clark zero plane is 10 mm above the Frankfurt zero. We then used the automated image registration (AIR) algorithm (Woods et al., 1992, 1993) in MEDx (Medical Image Processing, Sensor Systems Inc, Sterling, VA, USA) to perform an automated coregistration of all scans in a series. For some scans, we performed additional manual registration afterwards. The same registrations were performed on each of the corresponding angiography scans.

Strong signal changes arising from changes in blood flow, volume, and increasing water fraction (due to continuous IV infusion of saline during anesthesia) were eliminated by subtracting thresholded and coregistered angiography scans from the anatomical images. This procedure removes the signal associated with blood vessels and sinuses, which is in the range of the signal produced by the tracer (compare blood vessels and Mn^{2+} signal in axonal projection tract shown in Figure 1D, arrowhead), from the anatomical images.

Visual inspection of the images in cases 1 and 2 showed that the signal in clearly identifiable anatomic regions (specifically GPe and GPi) continued to increase over time. We performed unpaired t tests between a baseline scan and later time points, using a single uncorrected threshold ($p < 0.02$) to generate maps of significant intensity increases for the entire volume (see Figures 4A or 7B for an example of a statistical map superimposed on images from an anatomical scan). The statistical maps were used in conjunction with visually-identified, anatomical landmarks to define areas of significant signal increase, which were later used as regions of interest (ROIs) in the final analysis. The histological data in cases 1 and 2 were compared with the anatomical MRI scans and used to identify and label all anatomic regions that exhibited significant intensity increases. The 2D, anatomically defined regions in several consecutive MR images were used to define 3-dimensional regions of interest (3D ROIs) corresponding to anatomical structures. The size (number of voxels) of a 3D ROI was determined by analyzing the voxels within an anatomically defined region and selecting all voxels up to the anatomical extents of the structure or until they stopped showing an identifiable signal change. Thus, the 3D ROIs varied in size from $2 \times 2 \times 2$ (8 voxels) for the Habenular nucleus to $5 \times 5 \times 5$ (125 voxels) for the ventral striatum. We computed the average signal intensities and their standard deviations as a function of time for each 3D ROI identified as showing significant signal increase. In case 3, we identified all regions in the baseline scan that exhibited a signal increase in cases 1 and 2. The time course of the tracer signal in cases 1 and 2 was used as a reference to create groups of scans in cases 3 and 4 that were likely to large differences in manganese (Mn^{2+}) signal. Mean scans derived from these groups were used to create difference images that would have revealed any anatomical regions affected by the tracer over long periods of time that would not have existed in the short time course experiments in cases 1 and 2. The data in Table 2 indicate the maximum signal intensity change observed at each of the defined 3D ROIs for all cases. The initial signal intensity was normalized to 1.0, and all graphs (Figures 5B and 8) show normalized (fractional) signal changes.

Acknowledgments

This work was supported by the Max Planck Society and Riken Brain Science Institute. We thank A.H. Asiyabegum for histological assistance and D. Blaurock for help for English corrections and editing.

Received: March 18, 2002
Revised: April 25, 2002

References

Aertsen, A.M., and Gerstein, G.L. (1985). Evaluation of neuronal connectivity: sensitivity of cross-correlation. Brain Res. *340*, 341–354.

Alexander, G.E., Crutcher, M.D., and DeLong, M.R. (1990). Basal ganglia-thalamocortical circuits: parallel substrates for motor, oculomotor, "prefrontal" and "limbic" functions. Prog. Brain Res. *85*, 119–146.

Aschner, M., and Aschner, J.L. (1991). Manganese neurotoxicity: cellular effects and blood-brain barrier transport. Neurosci. Biobehav. Rev. *15*, 333–340.

Baizer, J.S., Ungerleider, L.G., and Desimone, R. (1991). Organization of visual inputs to the inferior temporal and posterior parietal cortex in macaques. J. Neurosci. *11*, 168–190.

Barbas, H., and Pandya, D.N. (1989). Architecture and intrinsic connections of the prefrontal cortex in the rhesus monkey. J. Comp. Neurol. *286*, 353–375.

Barbeau, A. (1984). Manganese and extrapyramidal disorders (a critical review and tribute to Dr. George C. Cotzias). Neurotoxicology *5*, 13–36.

Carmichael, S.T., and Price, J.L. (1994). Architectonic subdivision of the orbital and medial prefrontal cortex in the macaque monkey. J. Comp. Neurol. *346*, 366–402.

Cheng, K., Saleem, K.S., and Tanaka, K. (1997). Organization of corticostriatal and corticoamygdalar projections arising from the anterior inferotemporal area TE of the macaque monkey: a Phaseolus vulgaris leucoagglutinin study. J. Neurosci. *17*, 7902–7925.

Devito, J.L., and Anderson, M.E. (1982). An autoradiographic study of efferent connections of the globus pallidus in Macaca mulatta. Exp. Brain Res. *46*, 107–117.

Enochs, W.S., Schaffer, B., Bhide, P.G., Nossiff, N., Papisov, M., Bogdanov, A., Brady, T.J., and Weissleder, R. (1993). MR imaging of slow axonal transport in vivo. Exp. Neurol. *123*, 235–242.

Felleman, D.J., and Van Essen, D.C. (1991). Distributed hierarchical processing in the primate cerebral cortex. Cereb. Cortex *1*, 1–47.

Ferry, A.T., Ongur, D., An, X., and Price, J.L. (2000). Prefrontal cortical projections to the striatum in macaque monkeys: evidence for an organization related to prefrontal networks. J. Comp. Neurol. *425*, 447–470.

Flaherty, A.W., and Graybiel, A.M. (1993). Two input systems for body representations in the primate striatal matrix: experimental evidence in the squirrel monkey. J. Neurosci. *13*, 1120–1137.

Gibson, A.R., Hansma, D.I., Houk, J.C., and Robinson, F.R. (1984). A sensitive low artifact TMB procedure for the demonstration of WGA-HRP in the CNS. Brain Res. *298*, 235–241.

Gruetter, R. (1993). Automatic, localized in vivo adjustment of all first- and second-order shim coils. Magn. Reson. Med. *29*, 804–811.

Gullberg, G.T., Wehrli, F.W., Shimakawa, A., and Simons, M.A. (1987). MR vascular imaging with a fast gradient refocusing pulse

sequence and reformatted images from transaxial sections. Radiology *165*, 241–246.

Haber, S.N., Lynd-Balta, E., and Mitchell, S.J. (1993). The organization of the descending ventral pallidal projections in the monkey. J. Comp. Neurol. *329*, 111–128.

Haber, S.N., Kunishio, K., Mizobuchi, M., and Lynd-Balta, E. (1995). The orbital and medial prefrontal circuit through the primate basal ganglia. J. Neurosci. *15*, 4851–4867.

Haber, S.N., Fudge, J.L., and McFarland, N.R. (2000). Striatonigrostriatal pathways in primates form an ascending spiral from the shell to the dorsolateral striatum. J. Neurosci. *20*, 2369–2382.

Hazrati, L.N., and Parent, A. (1991). Contralateral pallidothalamic and pallidotegmental projections in primates: an anterograde and retrograde labeling study. Brain Res. *567*, 212–223.

Hazrati, L.N., and Parent, A. (1992). The striatopallidal projection displays a high degree of anatomical specificity in the primate. Brain Res. *592*, 213–227.

Hedreen, J.C., and DeLong, M.R. (1991). Organization of striatopallidal, striatonigral, and nigrostriatal projections in the macaque. J. Comp. Neurol. *304*, 569–595.

Henriksson, J., Tallkvist, J., and Tjalve, H. (1999). Transport of manganese via the olfactory pathway in rats: dosage dependency of the uptake and subcellular distribution of the metal in the olfactory epithelium and the brain. Toxicol. Appl. Pharmacol. *156*, 119–128.

Hoover, J.E., and Strick, P.L. (1999). The organization of cerebellar and basal ganglia outputs to primary motor cortex as revealed by retrograde transneuronal transport of herpes simplex virus type 1. J. Neurosci. *19*, 1446–1463.

Horsley, V., and Clark, R.H. (1908). The structure and functions of the cerebellum examined by a new method. Brain *31*, 45–124.

Ilinsky, I.A., and Kultas-Ilinsky, K. (1987). Sagittal cytoarchitectonic maps of the Macaca mulatta thalamus with a revised nomenclature of the motor-related nuclei validated by observations on their connectivity. J. Comp. Neurol. *262*, 331–364.

Ilinsky, I.A., Jouandet, M.L., and Goldman-Rakic, P.S. (1985). Organization of the nigrothalamocortical system in the rhesus monkey. J. Comp. Neurol. *236*, 315–330.

Johnson, T.N., and Rosvold, H.E. (1971). Topographic projections on the globus pallidus and the substantia nigra of selectively placed lesions in the precommissural caudate nucleus and putamen in the monkey. Exp. Neurol. *33*, 584–596.

Jones, E.G., and Powell, T.P.S. (1970). An anatomical study of converging sensory pathways within the cerebral cortex of the monkey. Brain *93*, 793–820.

Kuypers, H.G., and Ugolini, G. (1990). Viruses as transneuronal tracers. Trends Neurosci. *13*, 71–75.

Lee, J.H., Garwood, M., Menon, R., Adriany, G., Andersen, P., Truwit, C.L., and Ugurbil, K. (1995). High contrast and fast three-dimensional magnetic resonance imaging at high fields. Magn. Reson. Med. *34*, 308–312.

Lin, C.P., Tseng, W.Y.I., Cheng, H.C., and Chen, J.H. (2001). Validation of diffusion tensor magnetic resonance axonal fiber imaging with registered manganese-enhanced optic tracts. Neuroimage *14*, 1035–1047.

Logothetis, N.K., Guggenberger, H., Peled, S., and Pauls, J. (1999). Functional imaging of the monkey brain. Nat. Neurosci. *2*, 555–562.

Logothetis, N.K., Merkle, H., Augath, M., Trinath, T., and Ugurbil, K. (2002). Ultra-high resolution FMRI in monkeys with implanted RF coils. J. Neurosci. Methods, in press.

London, R.E., Toney, G., Gabel, S.A., and Funk, A. (1989). Magnetic resonance imaging studies of the brains of anesthetized rats treated with manganese chloride. Brain Res. Bull. *23*, 229–235.

Middleton, F.A., and Strick, P.L. (1994). Anatomical evidence for cerebellar and basal ganglia involvement in higher cognitive function. Science *266*, 458–461.

Middleton, F.A., and Strick, P.L. (1996). The temporal lobe is a target of output from the basal ganglia. Proc. Natl. Acad. Sci. USA *93*, 8683–8687.

Nauta, W.J., and Mehler, W.R. (1966). Projections of the lentiform nucleus in the monkey. Brain Res. *1*, 3–42.

Newland, M.C., Ceckler, T.L., Kordower, J.H., and Weiss, B. (1989). Visualizing manganese in the primate basal ganglia with magnetic resonance imaging. Exp. Neurol. *106*, 251–258.

Parent, A., and Hazrati, L.N. (1994). Multiple striatal representation in primate substantia nigra. J. Comp. Neurol. *344*, 305–320.

Parent, A., and Hazrati, L.N. (1995a). Functional anatomy of the basal ganglia. I. The cortico-basal ganglia-thalamo-cortical loop. Brain Res. Brain Res. Rev. *20*, 91–127.

Parent, A., and Hazrati, L.N. (1995b). Functional anatomy of the basal ganglia. II. The place of subthalamic nucleus and external pallidum in basal ganglia circuitry. Brain Res. Brain Res. Rev. *20*, 128–154.

Parent, M., Levesque, M., and Parent, A. (1999). The pallidofugal projection system in primates: evidence for neurons branching ipsilaterally and contralaterally to the thalamus and brainstem. J. Chem. Neuroanat. *16*, 153–165.

Parent, M., Levesque, M., and Parent, A. (2001). Two types of projection neurons in the internal pallidum of primates: single-axon tracing and three-dimensional reconstruction. J. Comp. Neurol. *439*, 162–175.

Pautler, R.G., and Koretsky, A.P. (2002). Tracing odor induced activation in the olfactory bulbs of mice using manganese enhanced resonance imaging (MEMRI). Neuroimage, in press.

Pautler, R.G., Silva, A.C., and Koretsky, A.P. (1998). In vivo neuronal tract tracing using manganese-enhanced magnetic resonance imaging. Magn. Reson. Med. *40*, 740–748.

Ragsdale, C.W., and Graybiel, A.M. (1981). The fronto-striatal projection in the cat and monkey and its relationship to inhomogeneities established by acetylcholinesterase histochemistry. Brain Res. *208*, 259–266.

Ryu, S., Brown, S.L., Kolozsvary, A., Ewing, J.R., and Kim, J.H. (2002). Noninvasive detection of radiation-induced optic neuropathy by manganese-enhanced MRI. Radiat. Res. *157*, 500–505.

Saint-Cyr, J.A., Ungerleider, L.G., and Desimone, R. (1990). Organization of visual cortical inputs to the striatum and subsequent outputs to the pallido-nigral complex in the monkey. J. Comp. Neurol. *298*, 129–156.

Saleem, K.S., and Tanaka, K. (1996). Divergent projections from the anterior inferotemporal area TE to the perirhinal and entorhinal cortices in the macaque monkey. J. Neurosci. *16*, 4757–4775.

Saleem, K.S., Suzuki, W., Tanaka, K., and Hashikawa, T. (2000). Connections between anterior inferotemporal cortex and superior temporal sulcus regions in the macaque monkey. J. Neurosci. *20*, 5083–5101.

Schwarz, C., and Bolz, J. (1991). Functional specificity of a long-range horizontal connection in cat visual cortex: a cross-correlation study. J. Neurosci. *11*, 2995–3007.

Seltzer, B., and Pandya, D.N. (1978). Afferent cortical connections and architectonics of the superior temporal sulcus and surrounding cortex in the rhesus monkey. Brain Res. *149*, 1–24.

Sidibé, M., Bevan, M.D., Bolam, J.P., and Smith, Y. (1997). Efferent connections of the internal globus pallidus in the squirrel monkey.1. Topography and synaptic organization of the pallidothalamic projection. J. Comp. Neurol. *382*, 323–347.

Sloot, W.N., and Gramsbergen, J.B. (1994). Axonal transport of manganese and its relevance to selective neurotoxicity in the rat basal ganglia. Brain Res. *657*, 124–132.

Smith, Y., and Parent, A. (1986). Differential connections of caudate nucleus and putamen in the squirrel monkey (Saimiri sciureus). Neuroscience *18*, 347–371.

Takeda, A., Kodama, Y., Ishiwatari, S., and Okada, S. (1998). Manganese transport in the neural circuit of rat CNS. Brain Res. Bull. *45*, 149–152.

Tjalve, H., Mejare, C., and Borg-Neczak, K. (1995). Uptake and transport of manganese in primary and secondary olfactory neurones in pike. Pharmacol. Toxicol. *77*, 23–31.

Tjalve, H., Henriksson, J., Tallkvist, J., Larsson, B.S., and Lindquist,

N.G. (1996). Uptake of manganese and cadmium from the nasal mucosa into the central nervous system via olfactory pathways in rats. Pharmacol. Toxicol. *79*, 347–356.

Toyama, K., Kimura, M., and Tanaka, K. (1981). Cross-correlation analysis of interneuronal connectivity in cat visual cortex. J. Neurophysiol. *46*, 191–201.

Van Everdingen, K.J., Enochs, W.S., Bhide, P.G., Nossiff, N., Papisov, M., Bogdanov, A., Brady, T.J., and Weissleder, R. (1994). Determinants of in vivo MR imaging of slow axonal transport. Radiology *193*, 485–491.

Walker, A.E. (1940). A cytoarchitectural study of prefrontal area of the macaque monkey. J. Comp. Neurol. *73*, 59–86.

Watanabe, T., Michaelis, T., and Frahm, J. (2001). Mapping of retinal projections in the living rat using high-resolution 3D gradient-echo MRI with Mn2+-induced contrast. Magn. Reson. Med. *46*, 424–429.

Wehrli, F.W., Shimakawa, A., Gullberg, G.T., and MacFall, J.R. (1986). Time-of-flight MR flow imaging: selective saturation recovery with gradient refocusing. Radiology *160*, 781–785.

Wiesel, T.N., Hubel, D.H., and Lam, D.M. (1974). Autoradiographic demonstration of ocular-dominance columns in the monkey striate cortex by means of transneuronal transport. Brain Res. *79*, 273–279.

Woods, R.P., Cherry, S.R., and Mazziotta, J.C. (1992). Rapid automated algorithm for aligning and reslicing PET images. J. Comput. Assist. Tomogr. *16*, 620–633.

Woods, R.P., Mazziotta, J.C., and Cherry, S.R. (1993). MRI-PET registration with automated algorithm. J. Comput. Assist. Tomogr. *17*, 536–546.

Zemanick, M.C., Strick, P.L., and Dix, R.D. (1991). Direction of transneuronal transport of herpes simplex virus 1 in the primate motor system is strain-dependent. Proc. Natl. Acad. Sci. USA *88*, 8048–8051.